Engineering Notes

Parameterizing the Search Space of Starshade Fuel Costs for Optimal Observation Schedules

Gabriel J. Soto,* Dmitry Savransky,† and Daniel Garrett‡
Cornell University, Ithaca, New York 14853
and
Christian Delacroix§
University of Liège, B-4000 Liège, Belgium

I. Introduction

STARSHADES are a promising concept for achieving the necessary level of starlight suppression needed to detect habitable zone exoplanets [1–3]. By deploying a separate spacecraft along the line of sight (LOS) of a space telescope to a target star, a shadow is cast onto the telescope pupil, blocking on-axis starlight while passing off-axis exoplanet light. Ensembles of end-to-end mission simulations produce posterior distributions of planet discoveries and the parameters of detected planets for specific mission designs [4,5]. For missions with a starshade, these simulations must incorporate the relevant dynamics, which increases computation time. Of the two main starshade flight modes of station keeping and retargeting between observations, the latter uses the most fuel and is our main focus [6–8]. The retargeting or slewing process creates a vast search space of trajectories: we can choose from any star on a target list and achieve alignment after an arbitrary slew time. At each decision step, the simulation scheduler must select the next best star to observe based on costs and the constraints of required integration times, evolving keepout regions, and mission goals [4,5,7,9,10].

Rather than solving a time-constrained optimization problem for each target at each decision step for each simulation, we can approximate the solution via various heuristics. Using simplified fuel cost models as in the work of Glassman et al. [7] or substituting the fuel cost with angular separation between stars as in the work of Savransky et al. [4] reduces the computation time but also accuracy. Kolemen and Kasdin [8] included the full dynamics in their simulations within a cost matrix: they precomputed individual trajectories from star i to star j in their target list and populated a static two-dimensional (2-D) matrix with fuel costs. Their cost matrix, however, was only computed for fixed slew times, whereas the

trajectory optimization requires more exploration of the time parameter due to dynamic constraints.

We propose a new parameterization of the cost matrix that both captures accurate fuel cost solutions and more adequately explores the constrained search space of possible slews. The parameterization is based on the slew time Δt and angular separation ψ between any two stars; the new cost matrix is sufficiently continuous that a 2-D interpolant can be used globally for any target list with only a small reduction in accuracy. We integrate this new parameterization within the Exoplanet Open-Source Imaging Mission Simulator (EXOSIMS) [5,10], which is a framework for end-to-end mission simulations, and show that examples of science yield results for different simulation ensembles.

II. Starshade Dynamical Model

A. Circular Restricted Three-Body Problem

We assume a space telescope on a nominal halo orbit about the sun–Earth L2 point [11,12]; the starshade trajectories about the halo are governed by the dynamics of the circular restricted three-body problem (CR3BP) [13]. A frame $\mathcal{R}$ (with orthogonal unit vectors $\hat{x}$, $\hat{y}$, and $\hat{z}$; Cartesian coordinates (x, y, z), and origin O at the barycenter of the primary masses) is defined to rotate with the two primaries relative to an inertial frame $\mathcal{I}$ with unit vectors $\hat{i}$, $\hat{j}$, and $\hat{k}$, as shown in Fig. 1.

The equations of motion for the third object (which is the starshade in this study) within this rotating frame are

$$\ddot{x} - 2\dot{y} = \frac{\partial \Omega}{\partial x} + f_{\text{SRP}} \cdot \hat{x} \tag{1}$$

$$\ddot{y} + 2\dot{x} = \frac{\partial \Omega}{\partial y} + f_{\text{SRP}} \cdot \hat{y} \tag{2}$$

$$\ddot{z} = \frac{\partial \Omega}{\partial z} + f_{\text{SRP}} \cdot \hat{z} \tag{3}$$

with

$$\Omega(x, y, z) = \frac{1}{2}(x^2 + y^2) + \frac{1 - \mu}{r_1} + \frac{\mu}{r_2} \tag{4}$$

$$r_1 = \sqrt{(\mu + x)^2 + y^2 + z^2} \tag{5}$$

$$r_2 = \sqrt{(1 - \mu - x)^2 + y^2 + z^2} \tag{6}$$

where $\Omega(x, y, z)$ is the effective potential due to the two primaries; r_1 and r_2 are the distances from the two primaries, respectively; and f_{SRP} is the solar radiation pressure (SRP) force. All units in this formulation are normalized as described by Koon et al. [13]. The reduced mass fraction μ is defined as the smaller primary mass scaled by the mass sum.

The SRP force acts on the starshade, which is modeled as an axisymmetric plate of cross-sectional area A with unit vector $\hat{n}$ defined normal to the surface [14]. An intermediate $\mathcal{P}$ frame [15] is defined along the sun–starshade vector r_1 as shown in Fig. 2, with

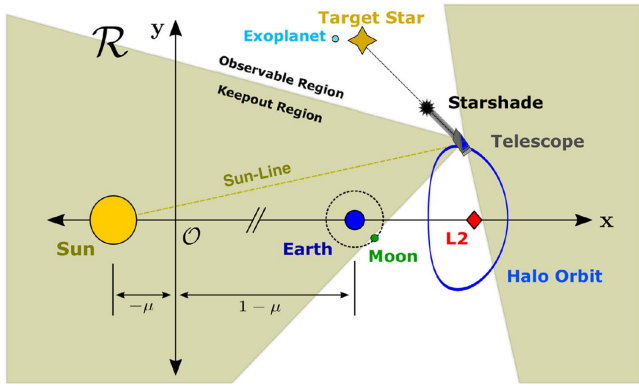$$\hat{p}_1 = \frac{r_1}{|r_1|} \tag{7}$$

Fig. 1   Diagram of the sun–Earth rotating frame in the ecliptic plane with locations of L2 and telescope–starshade–star configuration shown. Target stars outside the sun's keepout region are observable to the telescope.
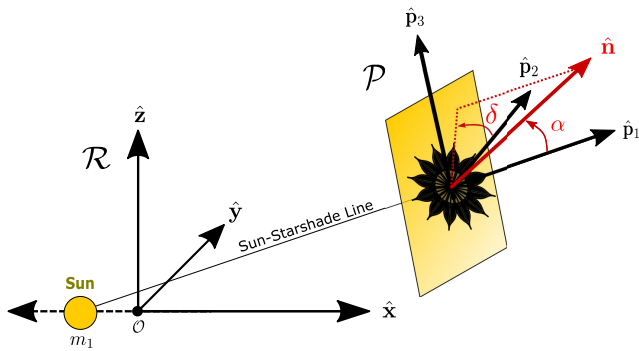

Fig. 2   Diagram of $\mathcal{R}$ and $\mathcal{P}$ frames used in equations of motion. $\mathcal{P}$ frame is defined perpendicular to the sun–starshade vector. Based on work of Dachwald et al. [15].

$$\hat{\boldsymbol{p}}_2 = \frac{\hat{\boldsymbol{z}} \times \hat{\boldsymbol{p}}_1}{|\hat{\boldsymbol{z}} \times \hat{\boldsymbol{p}}_1|} \qquad (8)$$

and

$$\hat{\boldsymbol{p}}_3 = \hat{\boldsymbol{p}}_1 \times \hat{\boldsymbol{p}}_2 \qquad (9)$$

The pitch and clock angles, α and δ, are defined as spherical angles relative to $\mathcal{P}$. The normal vector is then

$$\hat{\boldsymbol{n}} = \cos\alpha\,\hat{\boldsymbol{p}}_1 + \sin\alpha\cos\delta\,\hat{\boldsymbol{p}}_2 + \sin\alpha\sin\delta\,\hat{\boldsymbol{p}}_3 \qquad (10)$$

For the retargeting portions of the starshade mission, we assume no preferential attitude: on average, half of the starshade area faces the sun throughout the trajectory (or, equivalently, $\alpha = 60°$). The clock angle is assumed to be, on average, $\delta = 0°$.

The total force exerted on the starshade throughout its motion [15] is

$$\boldsymbol{f}_{\mathrm{SRP}} = 2PA\cos\alpha[b_1\hat{\boldsymbol{p}}_1 + (b_2\cos\alpha + b_3)\hat{\boldsymbol{n}}] \qquad (11)$$

where b_1, b_2, and b_3 are optical coefficients with values taken from Glassman et al. [7]. Integrating the full equations of motion with initial conditions in the vicinity of the nominal (precomputed) telescope halo orbit provides the motion of the starshade.

B.   Establishing Line of Sight

During station keeping, the size of the shadow cast onto the telescope pupil plane by the starshade depends on the triangle formed by d, the constant separation distance between the telescope and

starshade [8], and the starshade radius R_S. This defines a geometric inner working angle θ_I [1], which is the smallest angle from the telescope-starshade LOS an exoplanet can be situated before its light too gets suppressed by the starshade, given by

$$\tan\theta_I = \frac{R_S}{d} \qquad (12)$$

We assume values for the starshade radius and θ_I that, together, specify the separation distance.

The starshade begins the retargeting trajectory at a distance d along the LOS to target star i at time t_i; it ends at a distance d along the LOS to target j at time $t_j = t_i + \Delta t$, where Δt is the slew time [7,8]. More details can be found in the work of Soto et al. [9].

C.   Solving the Boundary Value Problem

The starshade positions are well defined at the endpoints of the retargeting trajectory but the corresponding velocities are not. This boundary value problem (BVP) is solved using Eqs. (1–3). We use similar methods as Kolemen and Kasdin [8]: the collocation algorithm `solve_bvp`, which is a Python implementation found in the `scipy` package [16]. A detailed explanation of our implementation was provided by Soto et al. [9]. The final continuous trajectory from the LOS of star i to the LOS of star j is depicted in Fig. 3. These solutions set the velocities at the start and end of the retargeting trajectory: $\boldsymbol{v}_{\mathrm{RT}}(t_i)$ and $\boldsymbol{v}_{\mathrm{RT}}(t_j)$ respectively.

D.   Calculating Fuel Cost

Changes in velocity at the transitions between station keeping and retargeting shown in Fig. 3 are modeled as impulsive maneuvers, which instantaneously change the velocity vector without altering the position vector. We quantify the fuel use by these velocity changes Δv. The velocity of the starshade in the inertial frame $^{\mathcal{I}}\boldsymbol{v}_{\mathrm{SK}}$ must match the inertial velocity of the telescope during station keeping [8], which is converted from the rotating to the inertial frames using rotation matrices defined by Koon et al. [13]. The retargeting
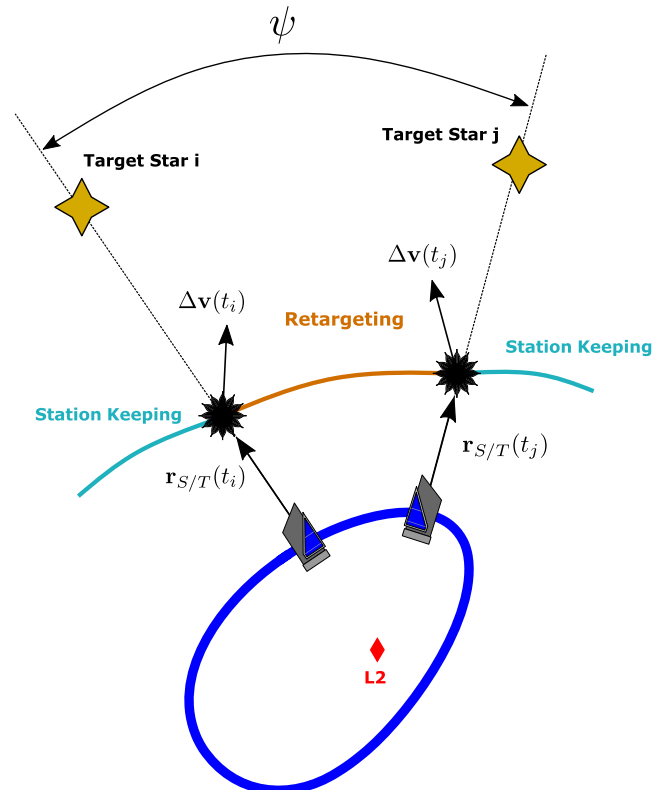

Fig. 3   Schematic of two starshade flight modes: station keeping with star i, retargeting to star j, and station keeping with star j. An angle ψ separates LOS vectors to the two stars.

velocities $\boldsymbol{v}_{RT}$ are similarly converted to inertial velocities (for more details, see the work of Soto et al. [9]). The Δv for each discrete jump is found by

$$\Delta v(t_i) = \|{}^{\mathcal{I}}\boldsymbol{v}_{RT}(t_i) - {}^{\mathcal{I}}\boldsymbol{v}_{SK}(t_i)\| \qquad (13)$$

$$\Delta v(t_j) = \|{}^{\mathcal{I}}\boldsymbol{v}_{RT}(t_j) - {}^{\mathcal{I}}\boldsymbol{v}_{SK}(t_j)\| \qquad (14)$$

where the superscript $\mathcal{I}$ is dropped for conciseness. The total Δv for a given retargeting maneuver from star i to star j for transfer time Δt initiated at t_0 is

$$\Delta v(i, j, \Delta t, t_0) = \Delta v(t_i) + \Delta v(t_j) \qquad (15)$$

We calculate fuel use Δm for a nominal chemical propulsion system via Tsiolkovsky's rocket equation [17]

$$\Delta m = m_0(1 - e^{-(\Delta v/g_0 I_{sp})}) \qquad (16)$$

where m_0 is the initial total mass, g_0 is the standard gravity constant, and I_{sp} is the specific impulse of the rocket engine. The starshade mass is sequentially decremented throughout the mission simulation as fuel is expended.

III.   Parameterizing Fuel Cost

A.   Fuel Cost Matrix

The total Δv for retargeting maneuvers, for a telescope on a predefined halo orbit and constant d, is a function of four parameters: the two stars i and j, the time t_0 at which the maneuver is initiated (i.e., where the telescope is located on the halo orbit), and the slew time Δt. One may choose to ignore some parameters to create feasible fuel cost heuristics: Kolemen and Kasdin [8] created cost matrices as functions of i and j but kept Δt and t_0 fixed. Ignoring the slew time parameter, however, prevents proper application of the time constraints required to properly simulate end-to-end missions.

B.   Sorting by Star Angular Separation

We create a new parameterization of the fuel cost matrix using the angular separation between stars. We define a unit vector for the location of each star in the inertial frames $\hat{\boldsymbol{r}}_{i/0}$ and $\hat{\boldsymbol{r}}_{j/0}$. The star angular separation $\boldsymbol{\psi}$ is

$$\psi = \text{sgn}(\hat{\boldsymbol{r}}_{j/0} \cdot \hat{\boldsymbol{k}}) \arccos(\hat{\boldsymbol{r}}_{i/0} \cdot \hat{\boldsymbol{r}}_{j/0}) \qquad (17)$$

The sign of the angular separation is taken with respect to the inertial frame to differentiate alignments with stars ahead of, or behind, the halo motion of the telescope, which require different amounts of fuel.

We consolidate the two dimensions of the previous $i - j$ cost matrix into a single dimension: an angular separation from the previously observed star. We populate the second remaining dimension with Δt: all possible slew times to align with a star at some separation ψ. The new 2-D cost matrix in Fig. 4 is generated at a specific t_0 relative to some reference star and shows substantially more continuity than previous parameterizations [8]. From the map, it is clear that the relationship between the two parameters is nonlinear. At small values of ψ, fuel costs increase with slew time: quick flights at short distances require less fuel. At large $\boldsymbol{\psi}$ values, fuel costs decrease with slew time: traversing large distances is easier with longer flights.

C.   Global Fuel Cost Interpolant

We exploit the continuity of the new fuel cost matrix with a two-dimensional interpolant. We use `interp2D`, which is a Python implementation found in the `scipy` package [16], using linear interpolation between points. A single cost matrix can be generated independently of the specific target catalog because only position
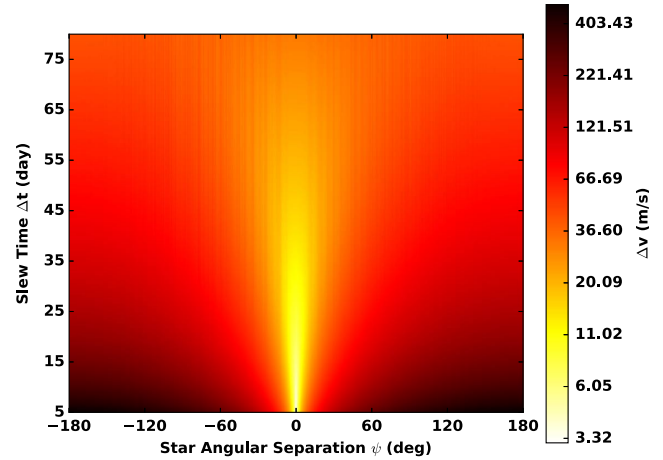

Fig. 4 Heat map of Δv as a function of both star angular separation ψ and slew time Δt. Interpolated values are shown. Color bar is shown in log scale.

vectors are needed to calculate angular separations. To reduce interpolation errors, we generate the Δv map using a fake catalog of stars with a compact distribution in ψ, which was described in the appendix of Soto et al. [9].

Two parameters are neglected with this approach: the time at which maneuvers are initiated t_0, and the location of the previous observed star. We conducted three separate tests to quantify the errors associated with these simplifications; in each, we generated multiple cost matrices where $\Delta v = f(\psi, \Delta t)$ and used a target list $\mathbb{T} \subset \mathbb{Z}$, which is a subset of integers. We computed each matrix at various t_0 taken at 20-day intervals throughout the ~6 month halo orbit period. In the first test, we selected a random pair of stars i_1 and $j_1 \in \mathbb{T}$ and calculated the true retargeting Δv for a range of Δt (ranging from 5 to 80 days in steps of 1 day), all initiated at a single t_0. We then compared the true fuel costs to interpolated values from all fuel cost matrices at different t_0 for the same star pairing. In the second test, we calculated the true Δv for a different random pair of stars $i_2 \in \mathbb{T}$ and $j_2 \in \mathbb{T}$ using the same Δt range and at every different t_0. We then compared this array of true fuel costs to interpolated results using a single fuel cost matrix generated at a single t_0. In the third test, we selected 50 random star pairs $\in \mathbb{T}$ at every t_0 and compared true and interpolated fuel cost values. The frequencies of the percent errors for each test are shown in Fig. 5. The mean absolute value percent error for interpolation was found to be under 10% for all tests, and it was approximately 2.53% for test 1, meaning that the derived cost matrix can be used as a target selection heuristic, as long as true fuel costs are then evaluated for the selected target. Generating trajectories of 195 realignments for slew times ranging from 5 to 80 days (in steps of 5 days) takes approximately 12 min on a dual-core 2.5 GHz processor. These calculations are now completed, with reasonable errors, within a fraction of a second using the new interpolant and parameterization, allowing for their inclusion in full mission simulations.

IV.   Scheduling with Time Constraints

A.   Dynamic Time Constraints

Mission time constraints are imposed on the global optimization problem by defining upper and lower bounds on the Δt axis of the cost matrix. A major time constraint is due to keepout regions [4,7]. A minimum keepout angle must be maintained between the telescope LOS and the direction of any bright object to avoid light contamination in the pupil. Light from a bright object can also reflect from the starshade into the telescope, requiring a maximum keepout angle from the telescope pointing. Solar panel pointing restrictions also limit the permissible telescope look vectors. Figure 1 shows the solar keepout region schematically.

The keepout zones evolve through time as the telescope moves along its orbit in an inertial frame. We define an observable window, which is the period of time when a star is continuously observable, via
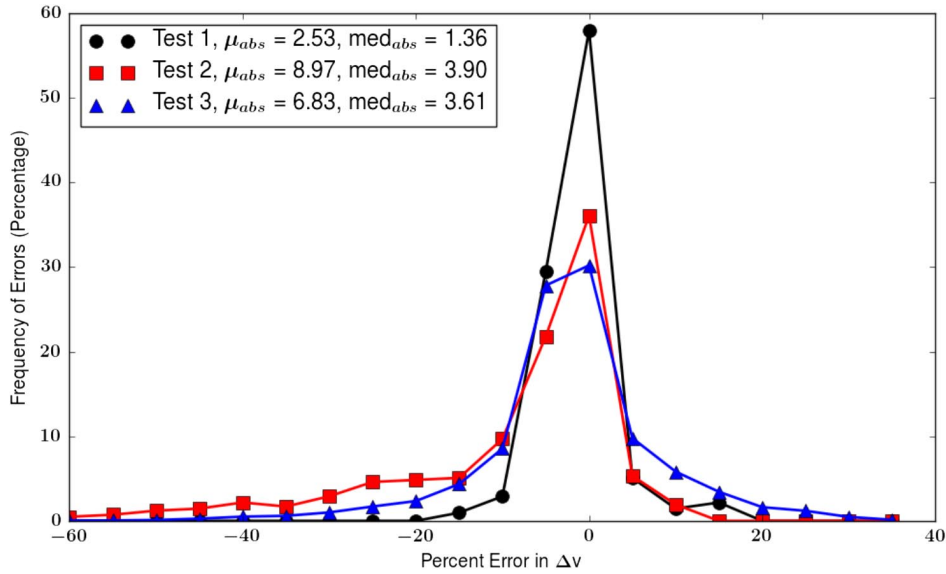
Fig. 5   Percent errors between true Δv values and interpolated values for three different test cases, shown as solid lines. Mean and median values are calculated from percent error absolute values.

a binary keepout map [4]. We precalculate angles β_b between the relative positions of the target star and all bright solar system bodies b (the sun, Earth, moon, etc.) throughout the entire mission and evaluate

$$45 \ \text{deg} < \beta_{\text{Sun}} < 90 \ \text{deg} \tag{18}$$

$$45 \ \text{deg} < \beta_{\text{Moon}} = \beta_{\text{Earth}} \tag{19}$$

$$1 \ \text{deg} < \beta_{\text{others}} \tag{20}$$

We populate the binary keepout map with the union of the preceding conditions. Figure 6 shows a sample keepout map over one year of mission time, with different colors representing the cause of a particular keepout. At each decision step in the mission simulation, we impose the observable time windows from the binary keepout map as upper and lower bounds on Δt for every star (at some ψ) within the interpolant. This allows us, for the first time, to combine strict time constraints with full CR3BP fuel cost solutions in end-to-end mission simulations.

B.   Exoplanet Open-Source Imaging Mission Simulator Implementation

We use EXOSIMS [5] to execute mission simulations: the next best star is sequentially selected for observation while time is still left in the mission and fuel still remains in the starshade. The original code has been modified to accommodate binary keepout maps and

2-D fuel cost interpolants: all prior to running simulations. Other time limits are also implemented, including integration times [10] and other mission-specific constraints. A more detailed review of the code updates is found in the work of Soto et al. [9].

We generate an ensemble of simulations using different schedulers [9]: a random walk scheduler that selects the next target at random from currently observable ones, a greedy scheduler choosing the target with the next highest completeness (probability that a star has a single orbiting exoplanet belonging to an assumed population and is observable by the instrument in question) [18,19], and a linear cost scheduler [4]. The last scheduler defines the cost function

$$\boldsymbol{c} = c_1 \Delta \boldsymbol{v}_{\text{min}} + c_2 (\boldsymbol{1} - \boldsymbol{C}_O) - c_3 \boldsymbol{f}_{\text{unv}} + c_4 \boldsymbol{f}_{\text{rev}} \tag{21}$$

where c_i are tunable weights; $\boldsymbol{c}$ is an $m \times 1$ vector of costs for the m stars in the filtered target list; $\Delta \boldsymbol{v}_{\text{min}}$ is a vector of the minimum fuel cost values for each m; $\boldsymbol{C}_O$ is a similar vector of completeness values; and $\boldsymbol{f}_{\text{unv}}$ and $\boldsymbol{f}_{\text{rev}}$ are factors that prioritize targets that have not been observed yet and targets deemed for a revisit, respectively. The linear cost scheduler selects the star corresponding to the root node of the minimum cost path in a truncated search of the tree of all possible future paths (see the work of Savransky et al. [4] for details). Previously, the c_1 term used a coarse heuristic for fuel costs given by just the angular separation of two targets, and so the new implementation is significantly better at capturing the true retargeting costs.
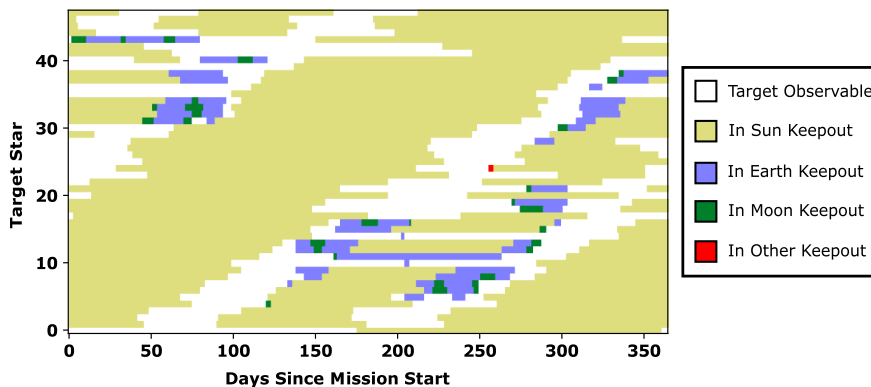

Fig. 6   Binary keepout map for a subset of stars on a target list.

Table 1   Mission parameters and assumptions

Parameter	Value
Mission time	3 years
Halo period	179 days
Pupil diameter	2.37 m
Δmag	22.5
Planet population	Kepler-like [21]
Total Δv	2094.33 m/s
Inner working angle	72 milliarcsecond
Starshade diameter	26 m
Separation distance	37,242.26 km
I_{sp}	308 s
Dry mass	1250 kg
Total mass	3500 kg

V.   Mission Simulation Results

The results of a mission simulation using the linear cost scheduler are shown in Fig. 7; assumptions and mission parameters are listed in Table 1 [20], which are similar to the Wide-Field Infrared Survey Telescope (known as WFIRST) mission [21]. Starshade parameters are taken from studies of the Exo-S mission [6]. Dry and total masses are estimated by assuming the launch vehicle capabilities of a Falcon 9 [22]. In this case, the schedule contains 29 total observations for the
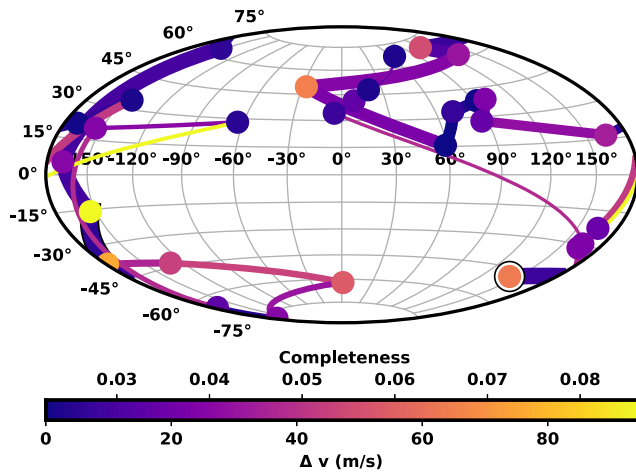

Fig. 7   Sample schedule generated using new observation scheduler for a starshade mission. Each circle represents the location of a different observed star.
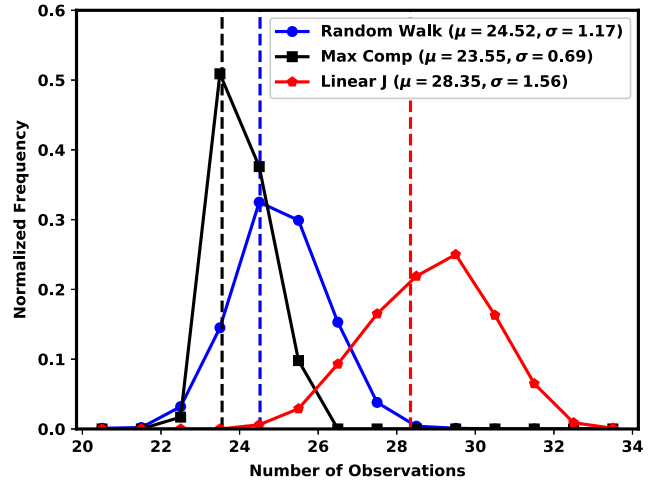

Fig. 9   Frequency of number of observations for three ensembles of 1000 mission simulations using a random walk, maximum completeness, and linear cost scheduler.

three-year mission; six led to positive detections, and three full spectral characterizations were completed.

Figure 7 shows observed target star positions as filled circles (in the equatorial coordinate system), with the circle color representing the completeness value of each target. The first observed target is marked with a bold border. Line colors denote the amount of Δv used for each retargeting slew; line thickness decreases as the mission progresses.

We conducted an ensemble of 1000 mission simulations, with each of the different selection schemes outlined in Sec. IV.B. Normalized yield frequencies and total observations are shown in Figs. 8 and 9. The linear cost function produced, on average, the most unique detections and conducted more observations due to more strategic fuel use.

VI.   Conclusions

A fuel cost interpolant based on full solutions to the circular restricted three-body problem starshade trajectories was presented, which effectively explored the slew time tradespace for any pair of targets. These efficient and fast approximations were also implemented within Exoplanet Open-Source Imaging Mission Simulator to perform ensembles of end-to-end exoplanet direct imaging missions for starshade-based imagers. The introduction of these accurate and fast dynamical fuel cost solutions was shown, in simulation, to increase both the total number of observations
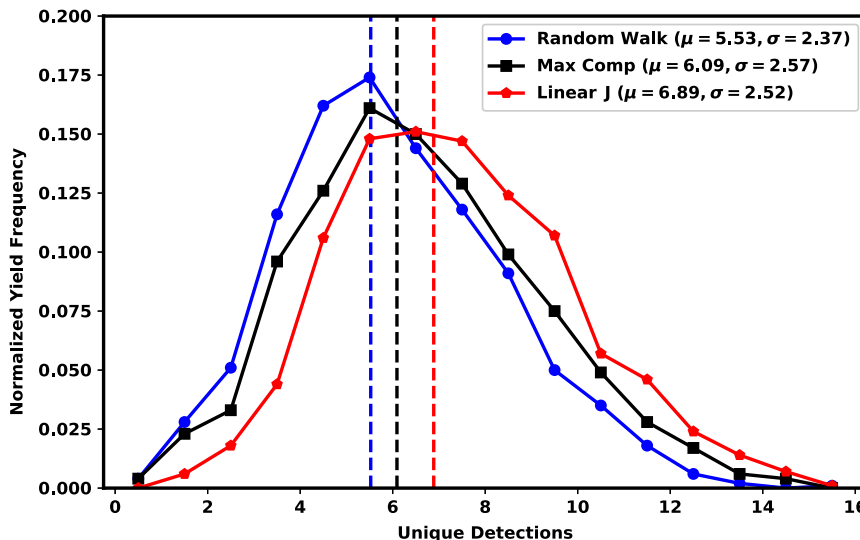

Fig. 8   Frequency of unique detections for three ensembles of 1000 mission simulations using a random walk, maximum completeness (Max Comp), and linear cost scheduler.

(because fuel is used more strategically) and the number of unique detections. These improvements have, for the first time, allowed us to realistically treat starshade fuel costs accurately in ensembles of end-to-end mission simulations, thereby greatly increasing our confidence in their results and improving their utility as a mission analysis and design tool. Although the focus was only on the case of chemical propulsion simulated through impulsive maneuvers, a future comparative analysis will be conducted on solar electric propulsion through continuous low-thrust maneuvers.

Acknowledgments

References

[1] Vanderbei, R. J., Cady, E., and Kasdin, N. J., "Optimal Occulter Design for Finding Extrasolar Planets," *Astrophysical Journal*, Vol. 665, No. 1, 2007, pp. 794–798.
    doi:10.1086/509297

[2] Des Marais, D. J., Harwit, M. O., Jucks, K. W., Kasting, J. F., Lin, D. N. C., Lunine, J. I., Schneider, J., Seager, S., Traub, W. A., and Woolf, N. J., "Remote Sensing of Planetary Properties and Biosignatures on Extrasolar Terrestrial Planets," *Astrobiology*, Vol. 2, No. 2, 2002, pp. 153–181.
    doi:10.1089/15311070260192246

[3] Smith, D., Warwick, S., Glassman, T. M., Novicki, M. C., Richards, M. C., Harness, A., and Patterson, K. D., "Measurements of High-Contrast Starshade Performance in the Field," *Space Telescopes and Instrumentation 2016: Optical, Infrared, and Millimeter Wave*, Vol. 9904, International Soc. for Optics and Photonics Paper 99043K, Bellingham, WA, 2016, pp. 1–12.
    doi:10.1117/12.2232841

[4] Savransky, D., Kasdin, N. J., and Cady, E., "Analyzing the Designs of Planet-Finding Missions," *Publications of the Astronomical Society of the Pacific*, Vol. 122, No. 890, 2010, pp. 401–419.
    doi:10.1086/652181

[5] Savransky, D., and Garrett, D., "WFIRST-AFTA Coronagraph Science Yield Modeling with EXOSIMS," *Journal of Astronomical Telescopes, Instruments, and Systems*, Vol. 2, No. 1, 2015, pp. 1–13.
    doi:10.1117/1.JATIS.2.1.011006

[6] Seager, S., et al., "The Exo-S Probe Class Starshade Mission," *Proceedings of SPIE 9605, Techniques and Instrumentation for Detection of Exoplanets VII*, Paper 96050W, Bellingham, WA, 2015, pp. 1–19.
    doi:10.1117/12.2190378

[7] Glassman, T., Newhart, L., Voshell, W., Lo, A., and Barber, G., "Creating Optimal Observing Schedules for a Starshade Planet-Finding Mission," *IEEE Aerospace Conference Proceedings*, IEEE Paper 11943925, Piscataway, NJ, 2011, pp. 1–19.
    doi:10.1109/AERO.2011.5747419

[8] Kolemen, E., and Kasdin, N. J., "Optimization of an Occulter-Based Extrasolar-Planet-Imaging Mission," *Journal of Guidance, Control, and Dynamics*, Vol. 35, No. 1, 2012, pp. 172–185.
    doi:10.2514/1.53479

[9] Soto, G., Keithly, D., Savransky, D., Delacroix, C., and Garrett, D., "Optimal Starshade Observation Scheduling," *Proceedings Volume 10698, Space Telescopes and Instrumentation 2018: Optical, Infrared, and Millimeter Wave*, SPIE Paper 106984M, Bellingham, WA, 2018, pp. 1–19.
    doi:10.1117/12.2311771

[10] Delacroix, C., Savransky, D., Garrett, D., Lowrance, P., and Morgan, R., "Science Yield Modeling with the Exoplanet Open-Source Imaging Mission Simulator (EXOSIMS)," *Proceedings Volume 9911, Modeling, Systems Engineering, and Project Management for Astronomy VI*, SPIE Paper 991119, Bellingham, WA, 2018, pp. 1–10.
    doi:10.1117/12.2233913

[11] Howell, K. C., "Three-Dimensional, Periodic, 'Halo' Orbits," *Celestial Mechanics*, Vol. 32, No. 1, 1984, pp. 53–71.
    doi:10.1007/BF01358403

[12] Farquhar, R. W., "The Utilization of Halo Orbits in Advanced Lunar Operations," NASA TN D-6365, 1971, pp. 1–99, https://ntrs.nasa.gov/archive/nasa/casi.ntrs.nasa.gov/19710021579.pdf [retrieved 2019].

[13] Koon, W. S., Lo, M. W., Marsden, J. E., and Ross, S. D., *Dynamical Systems, the Three-Body Problem and Space Mission Design*, 1st ed., Marsden Books, Pasadena, CA, 2011, pp. 23–167, http://www.cds.caltech.edu/~marsden/volume/missiondesign/KoLoMaRo_DMissionBk.pdf [retrieved 15 Nov. 2016].

[14] McInnes, C., *Solar Sailing: Technology, Dynamics and Mission Applications*, Springer-Praxis Books, New York, 1999, pp. 32–170.

[15] Dachwald, B., Mengali, G., Quarta, A. A., and Macdonald, M., "Parametric Model and Optimal Control of Solar Sails with Optical Degradation," *Journal of Guidance, Control, and Dynamics*, Vol. 29, No. 5, 2006, pp. 1170–1178.
    doi:10.2514/1.20313

[16] Jones, E., Oliphant, T., Peterson, P., et al., "SciPy: Open Source Scientific Tools for Python," 2001, https://www.scipy.org/citing.html.

[17] Turner, M. J. L., *Rocket and Spacecraft Propulsion: Principles, Practice and New Developments*, 3rd ed., Springer-Praxis Books, New York, 2009, pp. 135–164.

[18] Brown, R. A., "Single-Visit Photometric and Obscurational Completeness," *Astrophysical Journal*, Vol. 624, No. 2, 2005, pp. 1010–1024.
    doi:10.1086/apj.2005.624.issue-2

[19] Garrett, D., and Savransky, D., "Analytical Formulation of the Single-Visit Completeness Joint Probability Density Function," *Astrophysical Journal*, Vol. 828, No. 1, 2016, Paper 20.
    doi:10.3847/0004-637X/828/1/20

[20] Fressin, F., Torres, G., Charbonneau, D., Bryson, S. T., Christiansen, J., Dressing, C. D., Jenkins, J. M., Walkowicz, L. M., and Batalha, N. M., "The False Positive Rate of Kepler and the Occurrence of Planets," *Astrophysical Journal*, Vol. 766, No. 2, 2013, Paper 81.
    doi:10.1088/0004-637X/766/2/81

[21] Spergel, D., et al., "Wide-Field InfraRed Survey Telescope-Astrophysics Focused Telescope Assets WFIRST-AFTA 2015 Report," Vol. 1, Cornell Univ., Ithaca, NY, 12 March 2015, https://arxiv.org/abs/1503.03757 [retrieved 10 Jan. 2017].

[22] Falcon 9 Launch Vehicle–Payload User's Guide, Space Exploration Technologies Corp. (SpaceX), Hawthorne, CA, 2015, https://www.spacex.com/sites/spacex/files/falcon_users_guide.pdf [retrieved 21 March 2017].